

High Energy Nuclear Physics

“ Three quarks for Muster Mark!
Sure he has not got much of a bark
And sure any he has it’s all beside the mark.

— James Joyce
(Finnegans Wake)

According to cosmological theories, in its early stages the Universe was extremely hot and dense. In the first few microseconds, the energy density was so high that hadrons could not be formed and their fundamental constituents were in a deconfined state. When the energy density has decreased enough, a phase transition led to the formation of the ordinary matter.

High Energy Nuclear Physics (HENP) investigates the hot and dense nuclear matter and the properties of its phase transition into ordinary matter through the study of ultra-relativistic heavy-ion collisions. The aim is to improve our understanding of the behavior of the matter in extreme conditions and of the Universe at the beginning of its life.

1.1 QCD: the theory of the Strong Interaction

In 1964 M. Gell-Mann and G. Zweig proposed independently a model that could explain the existence of the great variety of hadrons discovered in the 1950s and 1960s [1-3]. This model, known as the Static Quark Model, was based on the assumption that hadrons are not fundamental particles, but they are composed states of elementary constituents called quarks. In this way it was possible to explain the large number of particles observed and their properties, which showed some sort of pattern, in term of constituents properties. Furthermore, thanks to the Static Quark Model, it was possible predict new hadrons (e.g. Ω^-) and to explain why certain particles don’t exist (e.g. baryons with $S = +1$). However, this model could not deal with many questions: why there is no evidence of free quarks? What hold quarks together in a hadron? Why the Δ^{++} baryon exists despite is forbidden by Pauli’s Principle? In order to answer these questions it was necessary to introduce

a new quantum number the colour [4]. The introduction of the colour led to the formulation of a quantum field theory for the Strong Interaction, inspired by the Quantum Electrodynamics (QED), the Quantum Chromodynamics (QCD).

The QCD is a non-Abelian quantum gauge theory, based on the invariance under local $SU(3)_c$ group transformations. The choice of this particular symmetry group is due to the hypothesis that the colour comes in three different states: red, blue and green. The local invariance under $SU(3)_c$ implies the existence of 8 massless gauge bosons mediators of the colour interaction, called gluons [5]. Therefore the QCD Lagrangian can be written as:

$$\mathcal{L}_{\text{QCD}} = \bar{\psi}_i (i(\gamma^\mu D_\mu)_{ij} - m \delta_{ij}) \psi_j - \frac{1}{4} G_{\mu\nu}^a G_a^{\mu\nu} \quad (1.1)$$

where the first term is related to quarks fields while the second is related to gluons fields. In the first term $\psi_i(x)$ represents the quarks fields expressed in the fundamental representation of $SU(3)_c$, while D_μ is the covariant derivative, defined as:

$$D_\mu = \partial_\mu - ig_s A_\mu^a \lambda_a. \quad (1.2)$$

In this derivatives shows up the coupling constant for the Strong Interaction g_s , the Gell-Mann matrices λ_α which gives a representation of the generators of $SU(3)_c$ symmetry group, and the gluon field $A(x)$. This first term of the QCD Lagrangian represents the quarks-gluons interaction via a QED-like vertex.

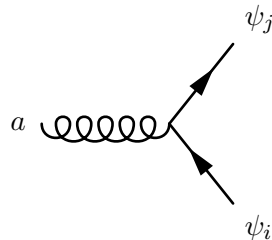


Fig. 1.1: Feynman diagram for the gluon-quarks interaction.

The second term of the Lagrangian $G_{\mu\nu}^a$ represents the gauge invariant gluon field strength tensor, and can be written as:

$$G_{\mu\nu}^a = \partial_\mu A_\nu^a - \partial_\nu A_\mu^a + g_s f^{abc} A_\mu^b A_\nu^c. \quad (1.3)$$

In this tensor $g_s f^{abc} A_\mu^b A_\nu^c$ is the non-Abelian part of the theory, which implies the self-interactions among gluons. These interactions have resulted from the fact that gluons carry a colour and an anti-colour charge, so they can interact among themselves. Therefore in addition to the QED-like vertex, in the QCD, 3 gluons and 4

gluons vertex are allowed at the tree level. The existence of the gluons vertex allows to have gluons loops.

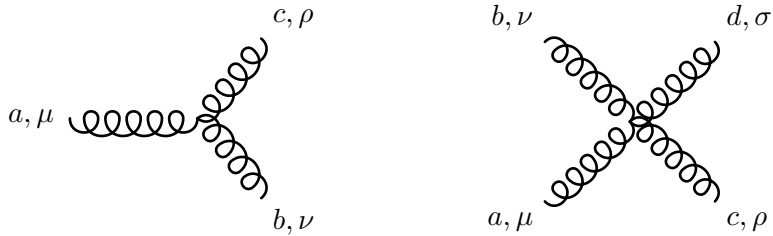


Fig. 1.2: Feynman diagrams for the gluon-gluon interactions at the tree level.

In the renormalization process of the theory, the non-Abelian nature of the QCD brings to the so-called *anti-screening* in colour interaction. Adding loop corrections to the gluons propagator, gluons loops contribute to the sum with opposite sign respect to the quarks loops. Therefore, in addition to the QED-like *screening* effect, there is an *anti-screening* effect due to gluons loops. As a result, the QCD shows up its specific features, *asymptotic freedom* and *confinement*.

Setting $\alpha_s = g_s^2/4\pi$ strong coupling constant can be written as [6]:

$$\alpha_s(Q^2) = \frac{\alpha_s(\mu^2)}{1 + \alpha_s(\mu^2)(33 - 2n_f) \ln(Q^2/\mu^2)} \quad (1.4)$$

where n_f is the number of quark families and μ is the renormalization scale of the theory. For high transferred momenta α_s goes to zero and the QCD becomes a free theory and this regime is called *asymptotic freedom*. At low Q^2 the Strong coupling diverges, forcing quarks to be strongly bound in hadrons: the so-called *confinement* regime. This behavior of the QCD coupling constant has been confirmed by experimental results over the years as shown in Figure 1.3. The equation 1.4 can be rewritten fixing the energy scale:

$$\alpha_s(Q^2) = \frac{12\pi}{(33 - 2n_f) \ln(Q^2/\Lambda_{\text{QCD}})} \quad (1.5)$$

where Λ_{QCD} is the renormalization scale of QCD (typically ≈ 200 MeV).

In QCD the perturbative approach used to calculate the elements of the scattering matrix (pQCD), is possible only for high Q^2 processes ($Q^2 \gg \mu^2$, thus $\alpha_s \ll 1$). As already mentioned, in low transferred momentum processes α_s diverges. Therefore, is impossible to express the elements of the scattering matrix in terms of power series expansion of the Strong coupling constant. In this regime it is still possible to evaluate the Green's functions of the QCD Lagrangian on a space-time lattice with spacing a , as proposed in 1974 by Wilson [7]. With this method, called lattice QCD

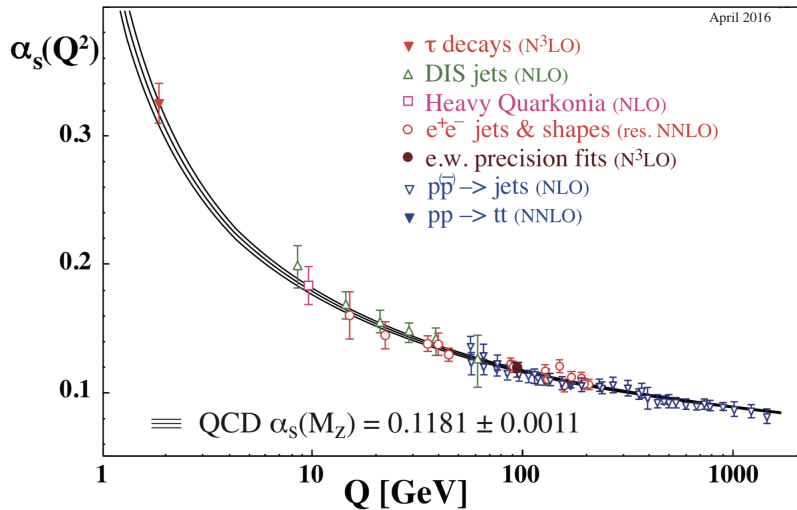


Fig. 1.3: Summary of measurements of α_s as a function of the energy scale Q [6].

(lQCD) is possible to extrapolate to the continuum ($a \rightarrow 0$) and get results to be compared with the experiments.

1.2 States of hadronic matter

One of the interesting consequences of the running coupling constant is the possibility of having different states of the hadronic matter. The state is essentially determined by the mean transferred momentum in the interactions which define the value of α_s . A system with low mean transferred momentum it is in the *confinement* regime, therefore quarks and gluons are required to be confined in hadrons. Otherwise in high mean transferred momentum systems, the *asymptotic freedom* regime allows the formation of a plasma where quarks and gluons are essentially free. This state of matter is called Quark Gluon Plasma (QGP) and is supposed that the universe was in this state in the first microseconds after the Big Bang. One of the main goals of the HENP is the study of the phase transitions between the different states of the hadronic matter.

Considering a system with finite dimensions, composed by hadronic matter, can be useful to describe it using thermodinamical variables like temperature (T) and chemical potential (μ). In this specific framework the chemical potential is interpreted as the energy required to create a baryonic state and it is called baryon chemical potential (μ_B). Figure 1.4 shows the phase diagram of the QCD matter predicted by the theory and the values of temperature T and baryon chemical potential (μ_B) which are accessible experimentally in high energy heavy ion collisions.

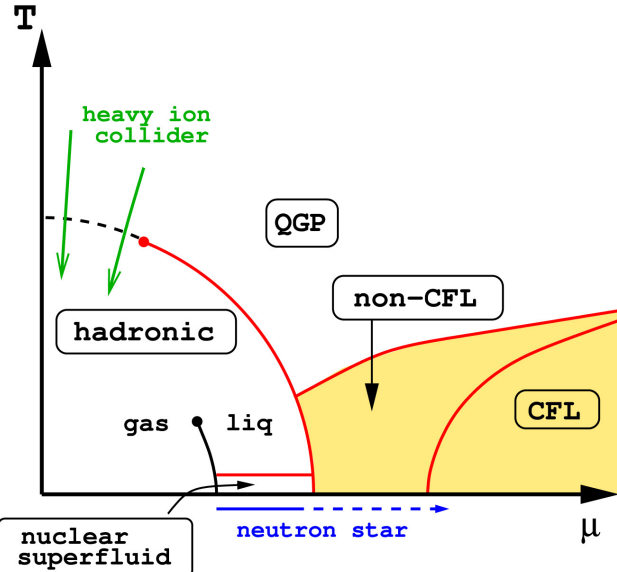


Fig. 1.4: Schematic representation of the nuclear matter phase diagram from [8]. QGP refers to the Quark Gluon Plasma state, CFL (Colour-Flavour Locked) corresponds to the colour superconducting phase that is present in systems with high baryon chemical potential. The green arrows represent the phase space investigated by collider experiments at the Relativistic Heavy Ion Collider (RHIC) and at the LHC.

The origin of the diagram ($T = \mu_B = 0$ GeV) corresponds to the QCD vacuum. At $T = 0$ GeV, μ_B is the energy required to create a baryonic state, therefore ordinary matter (proton, neutrons and nuclei) sits around 1 GeV on the μ_B axis. Along the μ_B axis lies a phase transition to a state, the Color Superconducting Phase, that has been hypothesized to be present in matter at high density, e.g. in the core of neutron stars [9]. Along the T axis, where $\mu_B = 0$, there is a phase transition when $T \gg \Lambda_{\text{QCD}}$. At this temperatures the average momentum exchange between quarks and gluons is so high that they reach the *asymptotic freedom*, hence they are no longer confined in colour singlets states. In these conditions they constitute a plasma of free coloured partons, similar to the primordial universe: the aforementioned QGP.

The order of the phase transition is determined by the behavior of the derivatives of the free energy of the system with respect to time. It basically describes how fast the free energy varies in a neighborhood of the transition temperature. A first order transitions takes place when a latent heat is present, leading to a discontinuous free energy first derivatives and variation of entropy. If no latent heat is involved in the process, occurs a second order transition. The free energy first derivative is continuous, while derivatives of higher than first order of the free energy are discontinuous. When the transition occurs with a continuous behavior of the free energy and its derivatives, it is called a *crossover* transition. In $\mu_B = 0$ conditions, the transition from hadron gas to the QGP takes place when $T \approx 150$ MeV with a *crossover* transition.

1.3 Heavy Ion Collisions

The QCD phase diagram is derived by theories and models, but their predictions are difficult to test. For the $T \approx 0$ GeV and high μ_B region, important suggestions can come from astronomic observations of neutron stars. For high T regions, instead, the only known way to cross the phase boundary between ordinary hadronic matter and QGP is by colliding ultrarelativistic heavy ions in the laboratory.

The journey of the High Energy Nuclear Physics started in the '70 at the Lawrence Berkeley National Laboratory where the first experiments on heavy ions collisions (HIC) was performed at modestly relativistic conditions (≈ 2 GeV/nucleon). In 1986, two HIC experiments started simultaneously at the Super Proton Syncrotron (SPS) at CERN and at the Alternate Gradient Syncrotron (AGS) at Brookhaven, colliding O ions at fixed target at higher energies. Nowadays the two main hadron colliders active with an HIC program and dedicated experiments are the Relativistic Heavy Ion Collider (RHIC) at the Brookhaven National Laboratory (BNL) and the Large Hadron Collider (LHC) at CERN.

1.3.1 The "Little Bang" at the LHC

Atomic nuclei are composite systems of nucleons with finite dimensions. When they collide at ultrarelativistic energies the problem of the description of the collision, that can be very complex, arises. The Glauber Model [10] is a semi-classical model describing nucleus–nucleus interaction in terms of nucleon–nucleon (NN) interactions. The Glauber Model is based on the assumption of the *optical limit*:

- nucleons are point like and independent inside the nuclei;
- only hadronic interactions are considered: protons and neutrons cannot be distinguished;
- the collision does not deflect colliding nucleons: they travel in a straight line;
- the cross section for an elementary nucleon-nucleon interaction is constant during the whole process.

With this assumption the Glauber Model allows a quantitative calculation of the interaction probability, the number of elementary NN collisions (N_{coll}), the number of the participants nucleons (N_{part}) and extension of the overlap region. These quantities are expressed in terms of the impact parameter \vec{b} , which characterizes the

collisions geometry. A direct experimental measurement of the impact parameter is precluded and the same goes for N_{coll} and N_{part} . However, the Glauber Model enables to correlate these variables with measurable quantities such as the total number of particles produced in the collision.

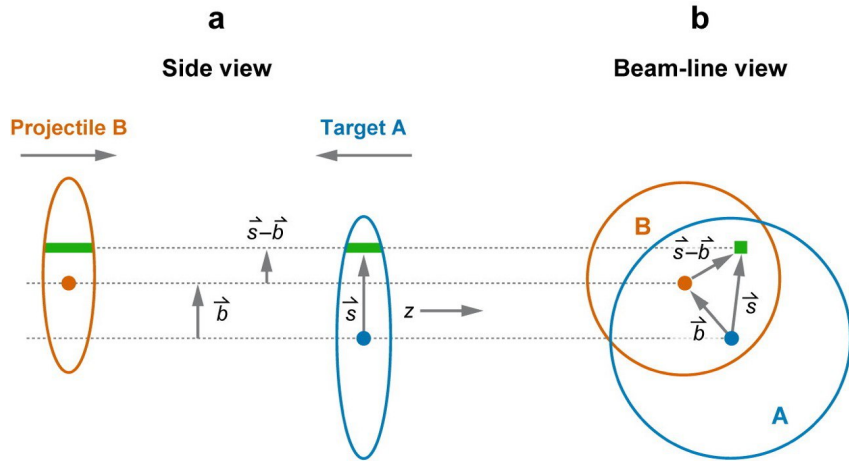


Fig. 1.5: Sketch of the longitudinal and transverse view of an heavy ion collision taken from [10]. In the side view, the colliding nuclei are squeezed to represent the Lorentz boost contraction due to their momentum.

Following the notation introduced in Figure 1.5 the nuclear overlap function for two colliding nuclei (A and B) can be written as:

$$T_{AB}(\vec{b}) = \int T_A(\vec{s}) T_B(\vec{s} - \vec{b}) d^2s \quad (1.6)$$

and represents the probability of finding a nucleon in both the colliding nuclei inside the overlap region in the transverse plane. $T_A(\vec{s})$ and $T_B(\vec{s} - \vec{b})$ are the *thickness functions* of the A and B nuclei. They represent the probability of finding a nucleon in the unit transverse area located at \vec{s} given the probability per unit volume $\rho(\vec{s}, z)$:

$$T(\vec{s}) = \int \rho(\vec{s}, z) dz. \quad (1.7)$$

As assumed, binary only interactions between nucleons are considered and the interaction does not deflect the trajectory of the interacting nucleons. Therefore, each nucleons can participate in more than one binary collision. The probability of having n binary collisions between the nuclei A and B, having A and B nucleons respectively, can be computed using the binomial statistics:

$$P(n, \vec{b}) = \frac{AB!}{n!(AB-n)!} [T_{AB}(\vec{b})\sigma_{inel}]^n [1 - T_{AB}(\vec{b})\sigma_{inel}]^{AB-n}. \quad (1.8)$$

From this expression the total inelastic cross section is obtained as a function of the impact parameter integrating the double differential cross section for two colliding nuclei:

$$\frac{d^2\sigma_{inel}^{AB}(b)}{db^2} = \sum_{n=1}^{AB} P(n, b) = 1 - [1 - T_{AB}(\vec{b}) \sigma_{inel}]^{AB} \quad (1.9)$$

$$\sigma_{inel}^{AB}(b) = \int_0^\infty 2\pi b db [1 - [1 - T_{AB}(\vec{b}) \sigma_{inel}]^{AB}] \quad (1.10)$$

From eq. 1.8, N_{coll} can be derived as a function of the impact parameter summing all the possible numbers of collisions weighted by their own probability and using the definition of the mean of the binomial distribution:

$$N_{coll}(b) = \sum_{n=1}^{AB} n P(n, b) = AB T_{AB} \sigma_{inel}. \quad (1.11)$$

Similarly N_{part} can be obtained by integrating over \vec{s} the contribution of the projectile nucleus and the contribution of the target nucleus as follow:

$$N_{part}(b) = \int d^2 s \{ A T_A(\vec{s}) [1 - (1 - T_B(\vec{b} - \vec{s}) \sigma_{inel})^B] + B T_B(\vec{b} - \vec{s}) [1 - (1 - T_A(\vec{s}) \sigma_{inel})^A] \} \quad (1.12)$$

In eq. 1.11 and 1.12, \vec{b} has been replaced with its norm as the direction of the vector is relevant for polarized nuclei only.

In spite of its simplicity, the Glauber Model allows to express N_{coll} and N_{part} starting from $\rho(\vec{s})$ and σ_{inel} . The main limitation is the usage of continuous density functions that implies considering discrete physical quantities as continuous.

1.3.2 Space time evolution of Heavy Ion collisions

When two ultrarelativistic atomic nuclei collide, high hadron density and high temperatures are produced in the impact region. In these conditions a long lived and strongly interacting system is created. The evolution of such a system, as well as the characterization of its properties, is very important to improve our understanding of the Strong interaction. Hence it is one of the main subject of investigation of HI experiments.

The space-time evolution of the system proceed in different phases. The current view on the evolution is summarized in Figure 1.6.

1. $t < 0$ fm/c: the two atomic nuclei travel in the beam line. In modern accelerators the nuclei are strongly Lorentz contracted in the beam line direction since they are at almost the speed of light (factor of 2700 at the LHC);

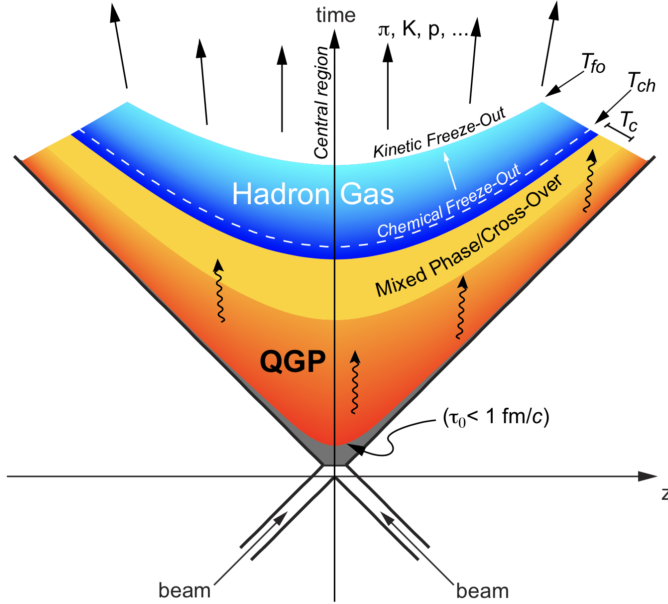


Fig. 1.6: Space-time representation of the evolution of the system created in a central Heavy Ion collision in the mid-rapidity region. The z direction is parallel to the beam line.

2. $t = 0 \text{ fm}/c$: collision time. The geometry of the collision can be described using the Glauber Model described in the previous section;
3. $0 < t \lesssim \tau_0 \sim 1 \text{ fm}/c$: in the early collision stages hard processes (i.e. process with high transferred momentum Q^2) occur between colliding partons. In this phase called *pre-equilibrium*, all the particles with high mass or/and high momentum are produced. In high energy collisions, as at the LHC, the nuclei constituent partons lose their energy in the mid-rapidity¹ region ($y \approx 0$) and then they escape at forward rapidities ($|y| \gg 0$). The escaping valence quarks bring the baryonic potential carried by the colliding nuclei at forward rapidity, vanishing the baryon chemical potential at mid-rapidity. The resulting system is an hot and dense medium. If the energy density is high enough, as at the LHC, a transition to the QGP state is expected. After a short strong parton rescattering phase, the obtained droplet of QGP matter reaches the equilibrium at his proper time τ_0 ;
4. $1 \lesssim t \lesssim 10 \text{ fm}/c$: the QGP droplet reach the thermal equilibrium and collectively expands under the push of the thermal pressure gradients generated at the system boundaries. Relativistic hydrodynamics models [11] are commonly used to describe the rapid expansion of the QGP matter, providing useful insights to interpret the experimental data. As a consequence of the expansion,

¹The rapidity is defined by Eq. 2.6 in Section 2.2.

the system cools down and the energy density decreases, transiting eventually from the Quark Gluon Plasma phase and ordinary hadronic matter;

5. $10 \lesssim t \lesssim 15 \text{ fm}/c$: the critical temperature between the two phases is reached. At this temperature the hadronization process starts, leading the system into an interacting *hadron resonance gas*. In this stage, the expansion and the cooling of the system continue, meanwhile elastic and inelastic interactions among the hadrons occur. When the energy density is decreased that much to not allowing inelastic interactions, the relative abundances of different particle species are fixed. The temperature at which the system stops to interact inelastically is called temperature of *chemical freeze-out* T_{ch} . After the *chemical freeze-out* only elastic processes took place, varying the particles momentum. When elastic interactions ends as well, the particles momentum spectra are fixed and this occurs at the temperature of *kinetic freeze-out* T_{kin} ;
6. $t \gtrsim 15 \text{ fm}/c$: hadrons created in the collision escape the interaction region with no further interactions. This regime is also known as *free hadron stream*.

The particles produced in the collisions and escaped from the interaction region are detected by the experimental apparaata carrying information about the environment in which they have been produced and about the medium in which they have travelled. In the following it will be shown how properties of the systems and characteristics of its evolution can be inferred by the measurement of particle production spectra and particle correlations.

1.4 Nuclei production in Heavy Ion collisions

The main subject of this thesis is the study of the $d^*(2380)$ dibaryon production at the LHC energies. Except for the deuteron, dibaryons are little known objects. In the next chapter, more details on what dibaryons are and what our understanding is about dibaryons, will be provided.

The (anti-)nuclei are loosely bound objects and it is not trivial how they can emerge from Heavy Ion collisions. The following sections are dedicated to a brief description of the major two classes of models that try to explain the nuclei and anti-nuclei production in HI collisions: the Statistical hadronization Models (SHMs) and the Coalescence model [12]. Dibaryons and in particular $d^*(2380)$ – which can be considered as an excited deuteron – should be subject of same production mechanisms as for (anti-)nuclei.

1.4.1 Statistical hadronization Models

The Statistical hadronization Models (also known as Thermal Models) was successfully developed in order to describe the abundances of different particle species produced in the collision between particles.

The general idea behind these models is that the final state of the interaction is composed by all the particle states compatible with the conservation laws imposed by the underlying theory of interaction (in our case the Standard Model of particle physics). The relative abundance of different particle states is set by the maximisation of the total phase space filled by the system, to which each particle species contributes according to its partition function. These models are of particular interest in HI collisions as the presence of an expanding medium that eventually reaches the thermal equilibrium seems appropriate for the statistical hadronization approach.

The system created in a relativistic HIC is large enough to be modelled using the Grand Canonical ensemble. This formalism can be used as the central rapidity region is in equilibrium with a thermal reservoir (the rest of the medium created in a HI collision) and quantities like energy, baryon number, charge and isospin are conserved on average. Most of the barrel experiments (as for ALICE central detectors) measure only this part of the phase space, hence the use of the Grand Canonical formalism is allowed. Within this formalism the parameters describing the equilibrium condition of a HIC include the temperature T and the baryon chemical potential μ_B . On this basis the partition function of the system can be written as:

$$Z(T, V, \mu) = \text{Tr} \left[e^{-\beta(H - \sum_i Q_i \mu_i)} \right] \quad (1.13)$$

with

$$\mu = \sum_i Q_i \mu_{Q_i} \quad \text{and} \quad \beta = \frac{1}{T} \quad (1.14)$$

where V is the volume of the system at equilibrium, H is the Hamiltonian and μ_{Q_i} is the chemical potential associated to the conserved quantum number Q_i . For a strongly interacting medium, the main conserved quantum numbers are the electric charge Q , the strangeness content of the system S and the baryon number B . The Hamiltonian H in the partition function is that one of a Hadron Resonance Gas since it is able to describe the behavior of a strongly interacting medium reproducing over a wide temperature range the equation of state obtained with lQCD calculations before the transition to a deconfined state. The choice of the mesonic, baryonic and resonance states included in the Hamiltonian depends on the implementation of the model and it determines the maximum temperature that can be described accurately.

The partition function of the system is the product of the contribution of all the particle states in the Hadron Resonance Gas:

$$Z(T, V, \mu) = \prod_i Z_i(T, V, \mu_i) \rightarrow \log Z(T, V, \mu) = \sum_i \log Z_i(T, V, \mu_i). \quad (1.15)$$

The partition functions are defined by the spin–statistics theorem:

$$\log Z_i(T, V, \mu_i) = \frac{Vg_i}{2\pi^2} \int_0^\infty \pm p^2 dp \log [1 \pm \lambda_i(T, \mu_i) e^{-\beta\epsilon_i}] \quad (1.16)$$

Bose-Einstein distribution for bosons (+) and Fermi-Dirac distribution for fermions (−). The g_i constant is the degeneracy state i and ϵ_i is the energy of one particle of the species i with momentum $p(\epsilon_i = \sqrt{p^2 + m_i^2})$. The dependence on the chemical potentials is encoded within the fugacity λ_i :

$$\lambda_i(T, \mu_i) = e^{\beta(B_i\mu_B + S_i\mu_S + Q_i\mu_Q)} = e^{\beta\mu_i} \quad (1.17)$$

where B_i , S_i and Q_i are the baryon number, strangeness content and electric charge associated with the particle species and μ_B , μ_S and μ_Q are the respective chemical potentials. As described in [13], expanding the logarithm and integrating over the momentum, the partition function for the species i becomes:

$$\log Z_i(T, V, \mu_i) = \frac{VTg_i}{2\pi^2} \sum_{k=1}^{\infty} \frac{(\pm 1)^{k+1}}{k^2} \lambda_i^k m_i^2 K_2(\beta km_i) \quad (1.18)$$

where the (+) is for bosons, the (−) for fermions and the K_2 is the second kind modified Bessel function of second order.

The average number of particle for the species i for a system described by the Grand Canonical ensemble, is defined as:

$$\langle N_i \rangle^{th}(T, V, \mu_i) = \frac{1}{\beta} \frac{\partial}{\partial \mu_i} \log Z_i(T, V, \mu_i) \frac{VTg_i}{2\pi^2} \sum_{k=1}^{\infty} \frac{(\pm 1)^{k+1}}{k} \lambda_i^k m_i^2 K_2(\beta km_i). \quad (1.19)$$

This equation does not fully describe the particle abundances measured in HI collisions. For the measured yields one should consider the feed-down contributions from all the other particle species (resonances) j in the thermal system that can decay strongly in a final state containing particles of the species i :

$$\langle N_i \rangle^{th}(T, V, \mu) = \langle N_i \rangle^{th}(T, V, \mu_i) + \sum_j \Gamma_{j \rightarrow i} \langle N_j \rangle^{th}(T, V, \mu_j) \quad (1.20)$$

where $\Gamma_{j \rightarrow i}$ is the decay rate of the state j into the final state i .

The definition of particle yields is valid in the limit of a low density system, where the repulsion interaction between the hadrons constituting the systems is negligible.

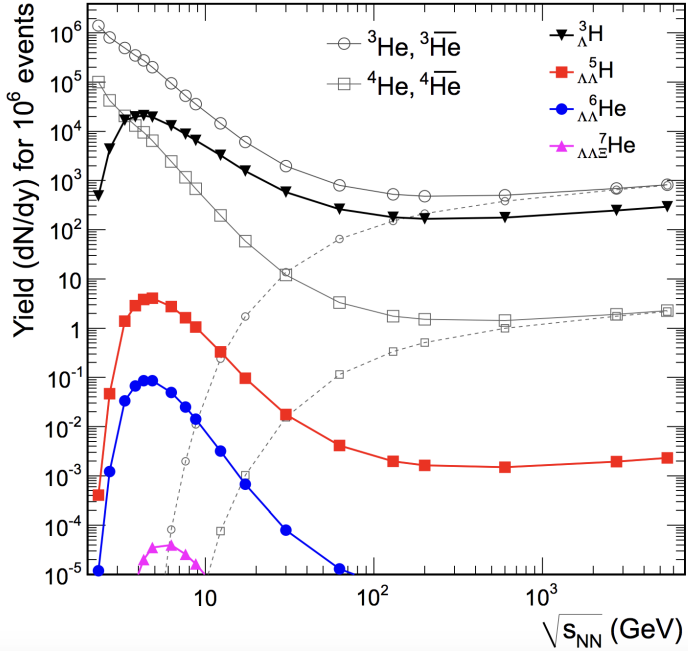


Fig. 1.7: Thermal model predictions for the production of various nuclei, anti-nuclei and hyper-nuclei as a function of the ion collision energy taken from [14]. At low collision energy the baryon chemical potential differs significantly from zero and the particle yield favours matter over anti-matter. As the energy increases, μ_B decreases and this difference vanishes.

The treatment of these interactions is still matter of active theoretical research. Nevertheless Eq 1.20 and 1.19 already indicate the crucial dependencies of the observed particle yields on the temperature T , volume V and the chemical potentials μ_B , μ_Q and μ_S .

Heavy Ions collisions no net strangeness is present in the colliding nuclei, thus $\mu_S = 0$, and μ_Q is fixed by the isospin asymmetry in the collision. Therefore two of the five parameters of the model are constrained by the collisions conditions. The baryon chemical potential μ_B is not constrained as the "amount of baryonic number" transported in the equilibrium region depends on the energy of the collision. The dependence on the volume V of the system can be removed looking at ratio between the yields of different particle species, which therefore depends only on the temperature of the system and on the baryon chemical potential. In the framework of the thermal models, light nuclei yields arise naturally when the chemical freeze-out temperature and the baryon chemical potential are set. A possible explanation on how the light nuclei can survive to the high temperature of the chemical freeze-out was pointed out in [14]: as the system expansion after the chemical freeze-out is supposed to conserve the entropy density, such conservation could be the steering mechanism for the nuclei production. From the fit of the particle abundances at lower energies, the authors of [14] predicted, using the thermal model, the yields of (anti-)nuclei at the LHC energy 1.7.

1.4.2 Coalescence Models

Coalescence models [12] represent a different theoretical approach developed to explain the measured light nuclei production in Heavy Ions collisions. These models address the problem guessing that light nuclei are created at the kinetic freeze-out. They are static models and there is no attempt to give a detailed description of the interactions that lead to their formation. The fundamental idea behind these predictions is that if nuclei constituents are close enough in phase space at the kinematic freeze-out they can bind to form a nucleus. The coalescence models make a prediction about the momentum distribution of the produced light nuclei as a function of the production spectra of the constituents.

The first coalescence model was developed to describe the deuteron formation in proton-nucleus collisions in 1961, in the following years has been extended to the production of various light nuclei in nucleus-nucleus collisions. The momentum spectrum for the i species related is linked to the proton momentum spectrum, which is used as a proxy of the constituent spectrum, by the following equation:

$$E_i \frac{d^3 N_i}{dp_i^3} = B_A \left(E_p \frac{d^3 N_p}{dp_p^3} \right)^A. \quad (1.21)$$

The proton spectrum is assumed to be identical to that one of the constituent neutron. One of the main reasons behind this generalization is that proton spectra are easier to measure in an experiment. These nucleon spectra are not those measured in the experiments, but the ones produced in the collision and not yet modified by the coalescence mechanism. The coalescence parameter B_A is interpreted as a function of the radius p_0 , that is the maximum distance at which coalescence can happen. In the simplest formulation of the coalescence models only the momentum space is considered (not the space-time), thus the coalescence parameter can be expressed neglecting the spin:

$$B_A = \left(\frac{4}{3} \pi p_0^3 \right)^{A-1} \frac{m_i}{m_p^A}. \quad (1.22)$$

where p_0 is the aforementioned radius and m_i and m_p are the nucleus and proton mass, respectively.

More sophisticated versions of this model predict a dependence on the geometry of the system and rely on different constituents momentum spectra and different formulation of the coalescence parameter B_A . Nevertheless, thanks to its simplicity and the presence of just one parameter p_0 , the most commonly used for the comparison with the data is the simple model briefly shown above.

The ALICE experiment

“ To see a World in a Grain of Sand
And a Heaven in a Wild Flower
Hold Infinity in the palm of your hand
And Eternity in an hour ”

— William Blake
(Auguries of Innocence)

The Large Hadron Collider (LHC) is the biggest and more powerful particle collider in the world. It consists of a 27 km ring of superconducting magnets and accelerating structures able to provide proton-proton and Lead-Lead collisions at the highest energies ever reached in laboratory to which the formation of the Quark Gluon Plasma is expected. While most of the LHC uptime is dedicated to the proton–proton physics that led to the discovery of the Higgs Boson [15, 16] and of two charmed pentaquark states [17], a significant part of the physics programme at the LHC is dedicated to heavy-ion physics and the characterization of the Quark Gluon Plasma.

2.1 The Large Hadron Collider

The Large Hadron Collider is the last element of the accelerator complex at CERN (Figure 2.1), a succession of machines that accelerate particles to increasingly higher energies. Each element in this chain boosts the energy of a beam of particles, before injecting it into the next machine. Protons and heavy ions are brought to their collision energies through different acceleration chains.

The protons injected in the LHC ring start their journey in the LINAC2, where ionized hydrogen atoms are accelerated up to 50 MeV. Then the beam is injected in the Proton Synchrotron Booster (PSB), which accelerates protons up to 1.4 GeV and provides the beam bunches to the Proton Synchrotron (PS). The Proton Synchrotron provides 25 GeV protons to the Super Proton Synchrotron (SPS), where they are accelerated up to 450 GeV before the injection in the LHC.

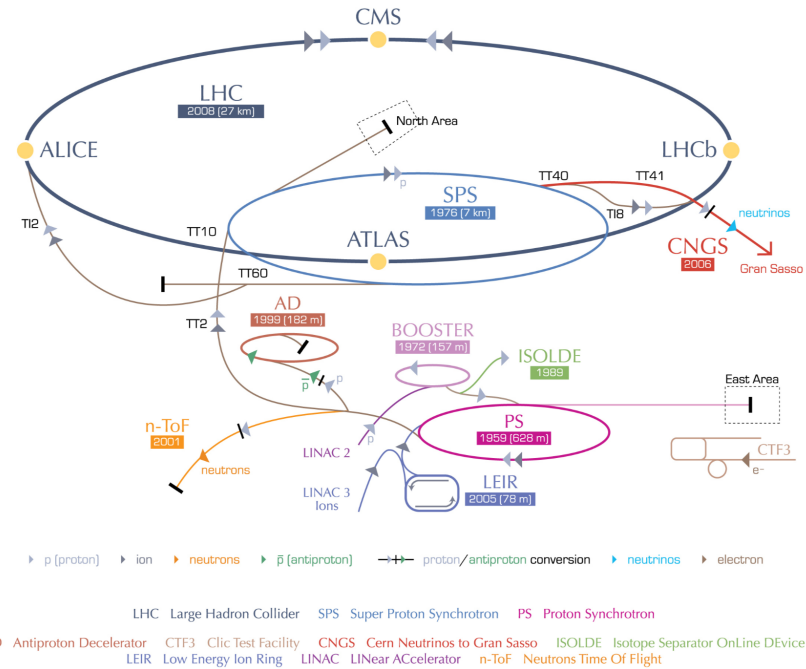


Fig. 2.1: Schematic view of the CERN accelerator complex and the LHC experiments [18].

Lead ions are produced from a highly isotopically pure ^{208}Pb sample heated to a temperature of about 800°C . The lead vapour is ionized by an electron current. Many different charge states are produced with a maximum around Pb^{29+} . These ions are selected and accelerated to 4.2 MeV/u (energy per nucleon) before passing through a carbon foil, which strips most of them to Pb^{54+} . The Pb^{54+} beam is accumulated, then accelerated to 72 MeV/u in the Low Energy Ion Ring (LEIR), which transfers them to the PS. The PS accelerates the beam to 5.9 GeV/u and sends it to the SPS after first passing it through a second foil where it is fully stripped to Pb^{82+} . The SPS accelerates it to 177 GeV/u then sends it to the LHC, which accelerates it to 2.56 TeV/u.

The LHC ring is composed by 1232 dipole magnets and 392 quadrupole magnets, which respectively guide and focus the counter-rotating beams in separate vacuum-filled pipes. When the beams are stable they are brought into collision in four interaction points corresponding to the major LHC experiments. The top centre-of-mass energy reached at the LHC in the collisions are 13 TeV and 5.02 TeV per nucleon pair for pp and Pb–Pb collisions respectively.

Besides the centre-of-mass energy another crucial parameter for a collider is the luminosity delivered to the experiment. Indeed the number of events per second generated in the LHC collisions can be evaluated with the following formula:

$$R_{\text{event}} = L \sigma_{\text{event}} \quad (2.1)$$

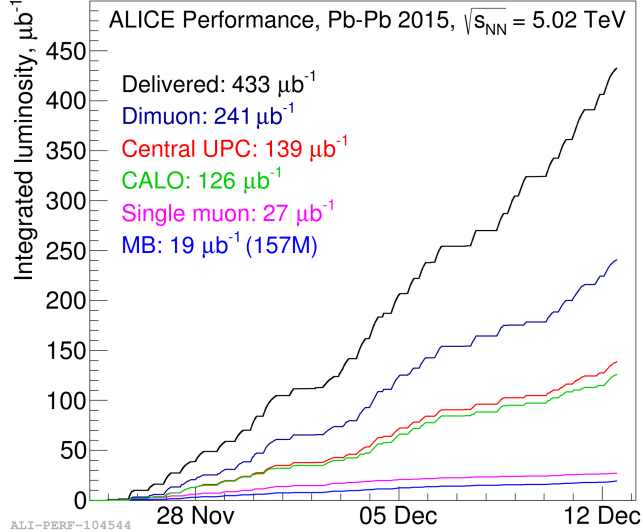


Fig. 2.2: ALICE delivered and integrated luminosity during the first Pb–Pb period in Run 2.

where L is the machine instantaneous luminosity and σ_{event} is the cross section for the event under study. The instantaneous luminosity depends only on the beam parameters and can be written as:

$$L = \frac{N_b N^2 f_{rev} \gamma}{4 \pi \epsilon_n \beta^*} F, \quad (2.2)$$

where N_b is the number of bunches in the collider ring, N is the number of charges in each bunch, f_{rev} is the revolution frequency of the beam, γ is the relativistic factor, ϵ_n is the normalized emittance¹ and β^* is the value of the amplitude function² at the interaction point (IP) where the luminosity is estimated.

In order to maximize the luminosity of the LHC, the option of a p–p̄ collider was excluded due to the problem of the anti–protons production that is very complicated. The LHC can store up to 2808 bunches, with $\sim 10^{11}$ protons per bunch, with 25 ns spacing [19]. The ALICE apparatus requires a peak luminosity of $L = 10^{27} \text{ cm}^{-2}\text{s}^{-1}$ in Pb–Pb collisions. Figure 2.2 shows the delivered luminosity by the LHC (black line) and the integrated luminosities collected by ALICE, for different trigger configurations (colored lines), during the first Pb–Pb period in Run 2 at the end of 2015.

A crucial information for the collider experiments is the position where the collision between the two beams takes place: the *primary vertex*. The nominal position of the primary vertex is the origin of the coordinate reference frame of the experiment. Nevertheless, due to the finite size of the bunches the position of the

¹ $\epsilon_n = \beta \gamma \epsilon$ where β and γ are the usual relativistic factors and the emittance ϵ is the spread of beam particles in the position-momentum phase space.

²The amplitude function $\beta(s)$ describes the beam amplitude modulation due to the changing focusing strength.

primary vertex fluctuates around the nominal position. Being $\sigma_{x,y,z}^{bunch}$ the *rms* of the bunch in the transverse and longitudinal direction, it can be shown that, assuming a gaussian profile of the bunches in the three directions, the *rms* of the vertex variation is:

$$\sigma_{x,y,z}^{vertex} = \frac{\sigma_{x,y,z}^{bunch}}{\sqrt{2}}, \quad (2.3)$$

where the *rms* size depends on the beam emittance and the amplitude function β^* :

$$\sigma_{x,y,z}^{bunch} = \sqrt{\frac{\epsilon_{x,y,z} \beta^*}{\sqrt{\pi}}}. \quad (2.4)$$

At the IP2, where the ALICE experiment is located, typical values for the vertex dispersion are $\sigma_{x,y}^{vertex} \sim 50 \mu\text{m}$ and $\sigma_z^{vertex} \sim 5 \text{ cm}$.

2.2 ALICE design

The main goal of the ALICE experiment is the study of the QCD matter created in high energy heavy ion collisions, hence has been specifically designed and optimized [20, 21] for this purpose. An heavy ion experiment must have an efficient tracking system with a large acceptance and a good particle identification (PID) capabilities in a wide momentum range, especially at low momentum. Furthermore, it must work in an environment characterized by a large charged particle multiplicity. At the time of ALICE design, the charged particles multiplicity per rapidity unit in central Pb–Pb collisions was predicted to range between 2000 and 8000 [22], and for this reason detectors with high granularity and low material budget have been developed [20, 21].

The current layout of the ALICE experiment is shown in Figure 2.3 while Table 2.1 lists the position and the purpose of the ALICE sub-detectors. The ALICE coordinate system is a right-handed orthogonal Cartesian system with the origin settled at the nominal beams interaction point. The x axis is aligned with the horizontal accelerator plane and points to the centre of the LHC, the y axis is perpendicular to the accelerator plane and points upward. As a consequence the z axis is parallel to the beam direction and its positive direction is defined by the chirality of the coordinate system. For a more useful description of the apparatus and the physical quantities, two other coordinates are defined, which together with the z axis described above, form a cylindrical coordinate system: the azimuthal angle ϕ increases counter-clockwise starting from $\phi = 0$ for x axis looking towards the CMS side, and the polar

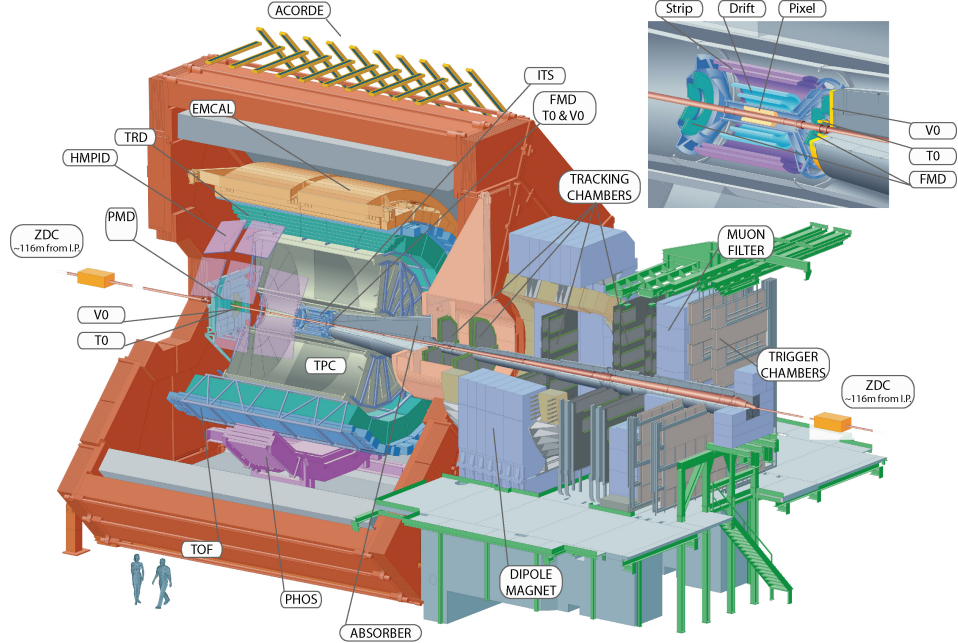


Fig. 2.3: The ALICE experimental setup and the red L3 solenoid magnet. The top right inset shows a zoom on the V0, T0, FMD and the ITS detectors.

angle θ increases from z ($\theta = 0$) to $-z$ ($\theta = \pi$). Other two useful variables, widely used in this thesis, are the *pseudo-rapidity* η :

$$\eta = \frac{1}{2} \ln \frac{|p| + p_z}{|p| - p_z} = -\ln \left[\tan \left(\frac{\theta}{2} \right) \right], \quad (2.5)$$

and *rapidity*:

$$y = \frac{1}{2} \log \left(\frac{E + p_z}{E - p_z} \right) \quad (2.6)$$

for a particle with four-momentum $p^\mu = (E, \vec{p})$, and the z axis parallel to the beam direction. For ultra-relativistic objects, the *pseudo-rapidity* numerically converges to the *rapidity*.

In the ALICE apparatus, three main parts can be distinguished: the *central barrel*, the *muon spectrometer* and the *forward detectors*.

Central Barrel Consists of all the detectors located in the pseudo-rapidity range $|\eta| < 0.9$ dipped in a solenoidal magnetic field ($B = 0.5$ T) produced by the warm resistive magnet previously used for the L3 experiment at LEP [24]. The central barrel tracking detectors include the Inner Track- ing System (ITS), the Time Projection Chamber (TPC) and the Transition Radiation Detector (TRD), covering the full azimuthal acceptance. This detectors, together with the Time Of Flight (TOF) detector and the High-Momentum Particle Identification (HMPID), provide also the information for particle identification (PID). There are also an ElectroMagnetic Calorimeter (EMCal) and a Photon Spectrometer (PHOS) dedicated to the physics of

Detector	Acceptance		Position	Main purpose
	Polar	Azimuthal		
SPD [†] layer 1	$ \eta < 2.0$	full	$r = 3.9 \text{ cm}$	tracking, vertex
SPD [†] layer 2	$ \eta < 1.4$	full	$r = 7.6 \text{ cm}$	tracking, vertex
SDD layer 3	$ \eta < 0.9$	full	$r = 15 \text{ cm}$	tracking, PID
SDD layer 4	$ \eta < 0.9$	full	$r = 23.9 \text{ cm}$	tracking, PID
SSD layer 5	$ \eta < 1.0$	full	$r = 38 \text{ cm}$	tracking, PID
SSD layer 6	$ \eta < 1.0$	full	$r = 43 \text{ cm}$	tracking, PID
TPC	$ \eta < 0.9$	full	$85 < r/\text{cm} < 247$	tracking, PID
TRD [†]	$ \eta < 0.8$	full	$290 < r/\text{cm} < 368$	tracking, e^\pm id
TOF [†]	$ \eta < 0.9$	full	$370 < r/\text{cm} < 399$	PID
PHOS [†]	$ \eta < 0.1$	$220^\circ < \phi < 320^\circ$	$460 < r/\text{cm} < 478$	photons
EMCal [†]	$ \eta < 0.7$	$80^\circ < \phi < 187^\circ$	$460 < r/\text{cm} < 478$	photons, jets
HMPID	$ \eta < 0.6$	$1^\circ < \phi < 59^\circ$	$r = 490 \text{ cm}$	PID
ACORDE [†]	$ \eta < 1.3$	$30^\circ < \phi < 150^\circ$	$r = 850 \text{ cm}$	cosmics
PMD	$2.3 < \eta < 3.9$	full	$z = 367 \text{ cm}$	photons
FMD	$3.6 < \eta < 5.0$	full	$z = 320 \text{ cm}$	ch. particles
	$1.7 < \eta < 3.7$	full	$z = 80 \text{ cm}$	ch. particles
	$-3.4 < \eta < -1.7$	full	$z = -70 \text{ cm}$	ch. particles
V0 A [†]	$2.8 < \eta < 5.1$	full	$z = 329 \text{ cm}$	ch. particles
V0 C [†]	$-3.7 < \eta < -1.7$	full	$z = -88 \text{ cm}$	ch. particles
T0 A [†]	$4.6 < \eta < 4.9$	full	$z = 370 \text{ cm}$	time, vertex
T0 C [†]	$-3.3 < \eta < -3.0$	full	$z = -70 \text{ cm}$	time, vertex
ZDC [†]	$ \eta > 8.8$	full	$z = \pm 113 \text{ cm}$	fwd neutrons
	$6.5 < \eta < 7.5$	$ \phi < 10^\circ$	$z = \pm 113 \text{ cm}$	fwd protons
	$4.8 < \eta < 5.7$	$ 2\phi < 32^\circ$	$z = \pm 113 \text{ cm}$	photons
MCH	$-4.0 < \eta < -2.5$	full	$-14.2 < z/\text{m} < -5.4$	muon tracking
MTR [†]	$-4.0 < \eta < -2.5$	full	$-17.1 < z/\text{m} < -16.1$	muon trigger

Tab. 2.1: Geometrical details and main purposes of the ALICE sub-detectors. This table has been taken and adapted from the description of the ALICE apparatus in [23]. The transverse (r) and longitudinal (z) coordinates as well as the acceptance (*polar* and *azimuthal*) are measured with respect to the ALICE coordinate reference frame, described in the text. When more than one position value is specified the detector is divided in two or several parts and the reported values are the minimum and maximum distances from the interaction point. The detectors marked with a dagger (\dagger) are also used for triggering.

high p_T photons and jets. Finally, on top of the ALICE solenoid, there is the ACORDE detector, an array of 60 large scintillators used to study the high-energy cosmic air showers.

Muon Spectrometer Located in the $-4 < \eta < -2.5$ region, is dedicated to the study of the spectrum of heavy-quark vector-mesons resonances. It consists of an absorber wall with small atomic number Z, a spectrometer with a dipole magnet, five tracking stations, four trigger stations and an iron absorber.

Forward Detectors Located in the forward-backward pseudorapidity regions and as close as possible to the beam line. They are: the Forward Multiplicity Detector (FMD), made of silicon strips detectors, the Photon Multiplicity Detector (PMD) and the Zero Degree Calorimeters (ZDC) consisting of two hadronic calorimeters, for protons and neutrons, plus one electromagnetic calorimeter. In addition there are two trigger detectors located at each side of the interaction point: the V0, made of scintillator detectors, and the T0, composed by two arrays of Cherenkov counters.

2.3 ALICE detectors

In the following sections more details on the detectors used for the study of the $d^*(2380)$ dibaryon production are provided.

2.3.1 Inner Tracking System

The Inner Tracking System (ITS) [22, 23] is a silicon tracker and is the detector closest to the interaction point. It is composed of six cylindrical layers of silicon detectors, carried out with three different technologies. In Figure 2.4 the layout of the Inner Tracking System is shown, while in Table 2.2 more details on the resolution and the geometry of the different layers are provided.

Silicon pixel detectors SPD are the two innermost layers of the ITS and are used for the determination of the primary vertex position as well as for the measurement of the impact parameter of secondary tracks. Furthermore, SPD, provides a quick trigger signal which contributes to the Level 0 trigger of the experiment.

Silicon drift detectors SDD are the two intermediate layers of the ITS. The technology used for the SDD allows high 2D resolution with limited number of read-out channels and the low material budget.

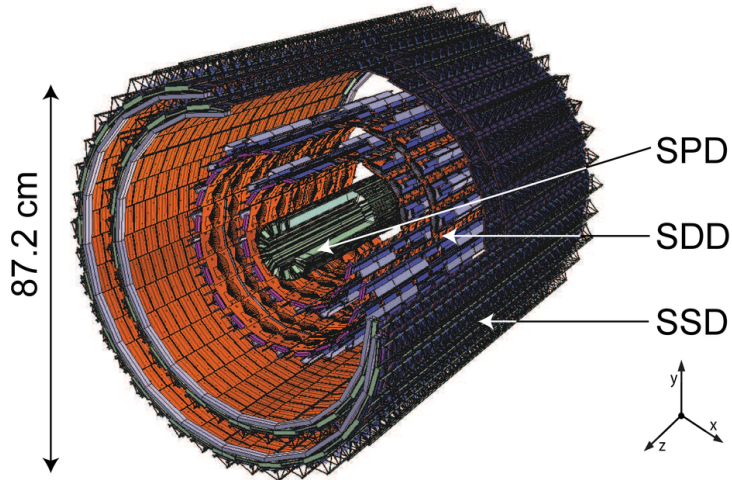


Fig. 2.4: Layout of the ALICE Inner Tracking System, with three different subdetectors.

Parameter	SPD	SDD	SSD
Material budget per layer ($\%X_0$)	1.14 - 1.14	1.13 - 1.26	0.83 - 0.86
Spatial resolution $r\phi$ (μm)	12	35	20
Spatial resolution z (μm)	100	25	830
Two track resolution $r\phi$ (μm)	100	200	300
Two track resolution z (μm)	850	600	2400
Active cell size (μm^2)	50×425	202×294	95×40000
Number of readout channels (k)	9835	133	2603

Tab. 2.2: Details about the material budget and spatial resolution of the ITS subdetectors [22]. The material budget is reported for each single layer.

Silicon strip detectors SSD are the outer layers of the ITS and are equipped with double sided silicon detectors, which provide a two dimensional measurement of the track position. The information of the SSD is crucial for the matching of the tracks from ITS to TPC, being the nearest layers to the TPC.

The main task of the ITS is the reconstruction of primary and secondary vertices, and the tracking of the low p_T particles. The first objective is achieved with a resolution better than $100 \mu\text{m}$, while for the second the ITS extends the tracking of the low p_T particles down to $p_T = 80 \text{ MeV}/c$, thanks to its high spatial resolution (Table 2.2) and low material budget. The total material budget of the ITS, keeping into account also the support structures and the thermal shields, is $7.18 \% X/X_0$. The SSD, together with the SDD, provide also the measurement of the energy loss of particles in their sensitive volume, extending the ALICE PID capabilities in the p_T region below $200 \text{ MeV}/c$.

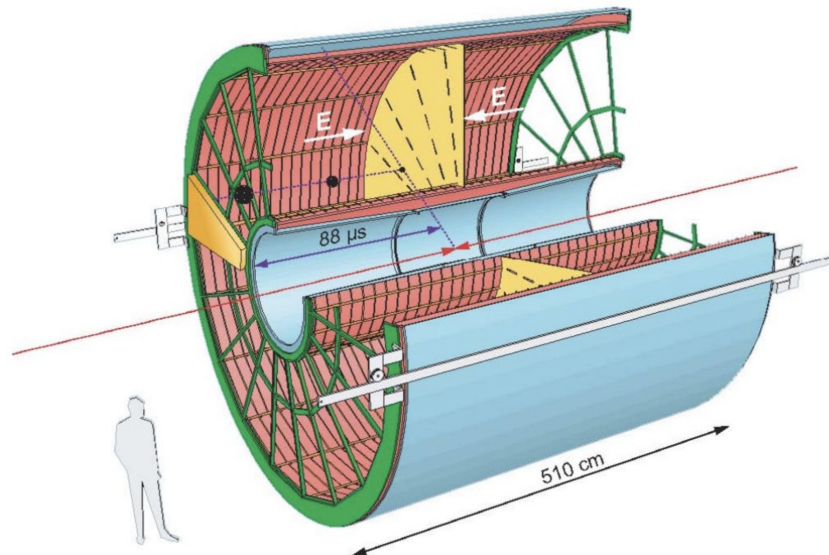


Fig. 2.5: Schematic layout of the ALICE Time Projection Chamber.

2.3.2 Time Projection Chamber

The Time Projection Chamber (TPC), illustrated in Figure 2.5, is the main ALICE tracking detector with good two-track separation. It is also one of the main PID detectors as it provides the information about the specific energy loss of the particles in its volume in a large momentum range.

The TPC, basically, is a 88 m^3 cylinder filled with gas and divided in two drift regions by the central electrode located at its axial centre. For the LHC Run 2 (2015-2018) the gas is mixture of Ar and CO₂. The field cage secures the uniform electric field along the z axis. Charged particles travelling in the TPC gas ionise the gas along their path, liberating electrons that drift towards the end plates of the cylinder. Each end plate is equipped with 36 readout chambers, which are organized in 18 sectors, covering 20° in azimuth each. The readout chambers consist in a system of multi-wire proportional chambers (MWPC) with cathode pad read-out. Each sector is segmented by pads organized in rows and the longitudinal coordinate is given by the drift time. Thanks to this segmentation, charged particles can be tracked and identified with up to 159 3-dimensional space points (TPC clusters), including also the specific energy loss information for the PID. The TPC radial position and acceptance are reported in Table 2.1.

2.3.3 Time Of Flight detector

The Time of Flight detector (TOF) has a cylindrical geometry and consists of a large area array of Multi-gap Resistive-Plate Chambers (MRPC). With a sensitive area of

$7.4 \times 120 \text{ cm}^2$ each and an intrinsic resolution of about $\sim 40 \text{ ps}$ [22], is used to identify charged particles and light nuclei in the momentum interval $0.2\text{--}4 \text{ GeV}/c$ in the central pseudorapidity range ($|\eta| < 0.9$). The time of flight of a particle is determined measuring the time between the event collision and the particle TOF hit cluster. The time of flight of the particle together with the momentum, obtained from the track curvature, allows to compute the particle β and, as a consequence, its mass. The precise determination of the event collision time, the so called t_0 , represents an important ingredient for the TOF PID and it is determined by using the information from the T0 detector as well as from the TOF.

2.3.4 T0 detector

The T0 detector consists of two arrays of Cherenkov counters placed on both sides of the interaction point along the z axis (Table 2.1). It is mainly used to determine the event collision time (t_0) with a resolution below 50 ps and independently from track and vertex reconstruction. The T0 information provides also the Level 0 trigger when the position of the vertex falls in appropriate intervals.

2.3.5 V0 detector

The V0 is a small angle detector consisting of two arrays (V0A and V0C) of 64 scintillators counters distributed in 8 rings and they are installed on both sides of the ALICE interaction point (Table 2.1). The V0 detectors are used to define the minimum bias (MB) trigger in ALICE and to determine the centrality in p–Pb and Pb–Pb collisions.

2.4 Trigger and Data Acquisition

The trigger system in ALICE is managed by the Central Trigger Processor (CPT) [25] which collects and synchronizes all the trigger inputs coming from all the triggering detectors with the information on the LHC filling scheme providing a trigger signal to the readout detectors in case of fulfilled trigger conditions. The Level 0 trigger (L0) decision is taken by using the fast detectors (SPD, V0, T0, EMCal, PHOS and muon trigger). The L0 signal arrives to the CTP in $1.2 \mu\text{s}$ after the collision. The signals from the detectors which are not fast enough for L0 trigger are collected in the level 1 (L1) trigger signal and sent to the CTP after $6.5 \mu\text{s}$. Finally the third level of trigger is sent after $88 \mu\text{s}$, which is the maximum drift time of electrons in the TPC, in order to help the rejection of the pile-up events in the TPC. The minimum-bias (MB) trigger selection in ALICE is defined by the logical "or" between the signals

of V0A, V0C and SPD detectors. This minimum-bias trigger is the one used in the analysis presented in this thesis.

The events passing all three trigger selections are sent both to the Data Acquisition (DAQ) machines and to the High Level Trigger (HLT).

The data fulfilling all the trigger requirements, are sent to the Local Data Concentrators (LDCs) through optical connections, the Detector Data Links (DDCs). LDCs is a farm of computers which build *subevents* from the event fragments they receive from the front-end electronics and then sends *subevents* to the Global Data Collectors (GDCs). The GDC compose the full event including information from the HLT. In the HLT level a fast reconstruction of the data – including clusterisation and track reconstruction – is performed, allowing further selections that are not possible in the hardware triggers. When the event building in the GDC is completed, the data are buffered in a local disk pool waiting to be transferred to the CERN computing centre, where they will be registered on tape.

2.5 ALICE offline framework

The offline analysis framework is fundamental for any High Energy Physics experiment. The huge amount of data collected by detectors requires a proper infrastructure able to process and analyse the reconstructed events. Beyond that, modern experiments need a large number of Monte Carlo simulations, for the development of the detectors, for performance studies, but also as a basis for physics analysis.

The infrastructure realized by the CERN in order to manage the LHC data flow is the Worldwide LHC Computing Grid (WLCG). The mission is precisely to provide global computing resources to store, distribute and analyse the \sim 50-70 Petabytes of data expected every year of operations from the LHC experiments.

The ALICE collaboration uses the WLCG resources for its simulations, event reconstruction and physics analysis. In the following section more details about this aspects of the ALICE operations will be provided.

2.5.1 Monte Carlo simulations

The first step of Monte-Carlo simulations is the event generation. The ALICE simulation tools include generators for all the interaction topologies provided for its physics program: pp, pA and heavy ion collisions. The event generator gives the set of all stable and weakly decaying particles produced in the collision, with their starting

kinematic parameters. The strongly decaying particles – as the $d^*(2380)$ dibaryon studied in this analysis – are usually handled at the generator level. The generated kinematic parameters are propagated, using a transport framework, through the experiment, whose geometry and material budget are precisely described in the ALICE software. Three different transport codes are available in the simulation framework: GEANT3, GEANT4 and FLUKA. These tools provide the information on the behavior of the transported particles through the sensitive part of the detector, giving the particle energy loss. This information converted in detectors electronics signal through the simulation of each detector response. Finally, the digitalized signal is stored in the same detector raw data format used in the real data taking and reconstruction.

2.5.2 Event Reconstruction

The ALICE event reconstruction flow starts from the raw data, collected or simulated, and is schematically shown in Figure 2.7.

In the first step of the event reconstruction the detector raw data are converted into clusters, through a set of algorithms which perform the reconstruction for each detector separately. All clusters are characterized by positions, signal amplitude and time. Other information, like the energy lost by the particle, the time of flight or the Cherenkov angle are attached to the clusters in the PID detectors allowing the identification of the tracked particle.

The second step of the reconstruction is a preliminary estimation of the position of the primary vertex using clusters in the SPD, the closest detectors to the interaction point. The first estimate of the primary vertex is fundamental to speed-up the tracking algorithm searching good candidate tracks, even if the final estimation of the position of the interaction vertex needs the full track information.

Subsequently, the Kalman filter technique [26] is used for performing track finding and fitting in TPC and ITS. The main tracking detector, in ALICE, is the Time Projection Chamber. Therefore track are reconstructed starting from the TPC, then they are prolonged in the ITS looking for matches with the ITS reconstructed tracks. The found tracks are backward propagated searching, also, for a possible match in the other central barrel detectors. Finally, the primary vertex can be determined using the fully reconstructed tracks.

The last step of the event reconstruction chain is the search for photon conversion and decays of strange hadrons.

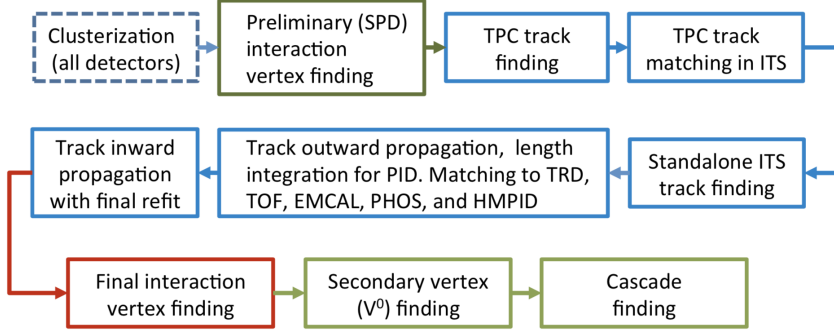


Fig. 2.6: Vertex and tracks reconstruction procedure in ALICE [23].

2.5.3 ALICE analysis framework

The ALICE software infrastructure, that allows the access to the collected and simulated data available everywhere on the grid, is the Alien (ALICE Environment) [27] grid middleware. Through the Alien user interface it is possible to launch the analysis tasks singularly on ALICE data. When more users are interested in analyzing the same data sample, is possible to use an optimized access pattern, called *analysis train*, which allows to run together all the tasks of those users in the same jobs. It defines a standard analysis flow in the ALICE experiment and it ensures the reproducibility of the analyses.

The data collected by the ALICE experiment are stored in binary files using the ROOT framework data format. The ALICE software environment is *AliRoot*, introduced in 1998 and based on the ROOT framework [28]. The analysis related code – containing all the software used in physics analysis – is collected in a part of the ALICE offline framework denominated *AliPhysics*. The reconstructed events are stored in two different formats: the Event Summary Data (ESD) format, that is mainly used for calibration and detector performance studies, and the Analysis Object Data (AOD) format, which contains only the relevant information at the analysis level.

2.6 ALICE performances

The ALICE experiment was specifically designed for the demanding experimental environment of the Pb–Pb collisions. One of the most challenging tasks, in these conditions, is the precise reconstruction of both momentum and origin of the particles produced. In this section the tracking and vertexing performances of the ALICE experiment will be presented, as well as the methods used for the particle identification.

2.6.1 Tracking

The importance of the tracking process lies in its relation with the particle momentum measurement and with the vertexing (Section: 2.6.2).

The momentum of a charged particle travelling in magnetic field is related to the radius of curvature of the particle track. Therefore, measuring the radius of curvature, it is possible to measure the particle momentum. In particular, in colliders experiments, the interaction point is surrounded by cylindrical position-sensitive detectors located in magnetic field – usually parallel to the beam axis – which provide a measurement of the *sagitta* of the track. The particle momentum is related to the sagitta by the following expression:

$$p = \frac{L^2 q B}{8 s}, \quad (2.7)$$

where L is the lever arm length of the tracking detectors, q is the charge of the particle and B the magnetic field. Therefore, the resolution on the particle momentum does not depend only on the magnetic field used, but also on L and, of course, on the resolution on the sagitta σ_s :

$$\frac{\sigma_p}{p} \propto p \frac{\sigma_s}{B L^2}. \quad (2.8)$$

Thanks to the large radial coverage ($0.039 \leq r \leq 3.680$ m), despite the mild solenoidal magnetic field, the ALICE apparatus is able to reconstruct tracks over a wide momentum range.

The first stage of the tracking algorithm starts building the track seeds at a large radius of the TPC. The seeds are propagated inward looking for other TPC cluster compatible with the track. Whenever a compatible cluster is found the track parameters are updated using a Kalman filter [26]. Different seeds can reuse the same cluster, therefore it is not uncommon to have two or more tracks sharing some clusters. If the fraction of shared clusters is above a predefined threshold (between 25% and 50%), a dedicated algorithm rejects the candidate tracks with the worst parameters quality. The tracks with at least 20 clusters (out of a maximum of 159) and that miss no more than 50% of the expected clusters are accepted and propagated to the inner radius of the TPC. Figure ?? shows the track reconstruction efficiency in the TPC.

The reconstructed TPC tracks are propagated to the SSD, the outermost layer of the ITS. At this point, the tracking algorithm in ITS proceeds with a procedure similar to that adopted for the TPC. Starting from the second layer of SSD, the seeds are propagated inward, penalizing tracks for which a compatible cluster in the extrapolation is not found. Among the prolongation candidates of the TPC track is

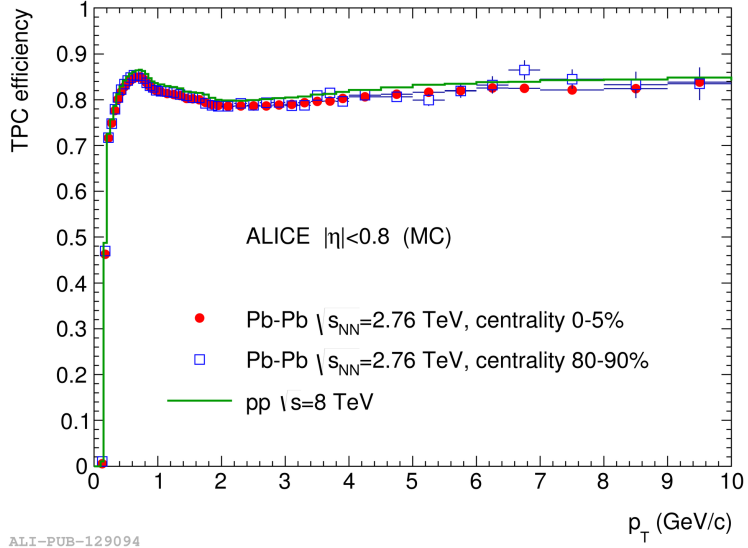


Fig. 2.7: TPC track reconstruction efficiency in pp (green line) collisions at $\sqrt{s} = 8$ TeV and for central (red dots) and peripheral (blue open square) Pb-Pb collisions at $\sqrt{s_{NN}} = 2.76$ TeV. The drop for $p_T \leq 0.5$ GeV/c is due to energy loss in the detector material and the shape at higher p_T is related to the loss of clusters in the dead zones of the TPC. The efficiency does not depend on the detector occupancy.

selected the one with the highest quality. This track is stored in the reconstructed event as ITS+TPC track.

The second stage of the tracking algorithm is the backward refit of the ITS+TPC tracks using the Kalman filter. The track is backward propagated looking for matching with TRD tracklets. If the matching is successful, updates the track parameters using the TRD tracklet information. During this process, at each step, the integrated track length and the expected time of flight for different particle species are computed and the related track parameters are updated. This information is used for a correct particle identification in the Time Of Flight detector (Section: 2.6.3). Then an attempt to extrapolate the track and match it to one of the TOF clusters is performed. The track length integration and time of flight calculation are stopped at this stage. Finally a further extrapolation is performed to match the track with other external central barrel detectors as HMPID, PHOS and EMCal.

The final stage of the track reconstruction, consists in propagating all the tracks from the TRD back to the innermost ITS layer. In each detector (TRD, TPC and ITS) the tracks are refitted using the information of all attached clusters. If the refit process goes well the track *refit flag* is switched on. At this stage the track's position, direction, inverse curvature and its associate covariance matrix are determined.

Following the described process the ALICE apparatus can reconstruct track with resolution between 1% and 10% in the momentum range from 0.1 to 100 GeV/c.

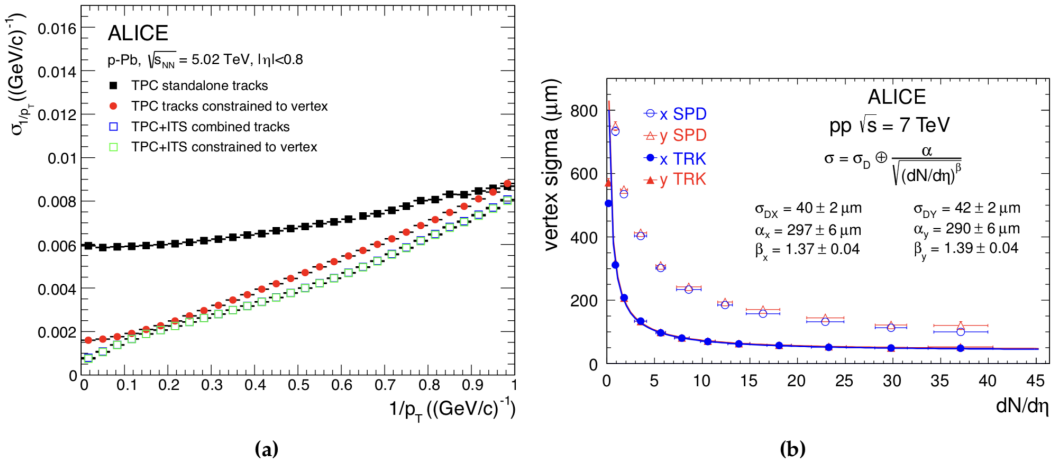


Fig. 2.8: Panel (a): p_T resolution for standalone TPC (black and red markers) and ITS+TPC (blue and green open squares) tracks with and without constraint to primary vertex in p–Pb collisions. Panel (b): Vertex resolution in the transverse plane using the SPD clusters only (open markers) or the full track information (full markers).

Figure 2.8a shows the $1/p_T$ resolution for standalone TPC and ITS+TPC tracks which is related to the p_T resolution by the formula:

$$\frac{\sigma_{p_T}}{p_T} = \frac{\sigma_{1/p_T}}{1/p_T}. \quad (2.9)$$

The effect of constraining the tracks to the primary vertex is shown as well and considering, for instance, TPC standalone tracks the resolution is reduced from 6% to 2% at low p_T by this requirements.

2.6.2 Vertexing

Primary vertex reconstruction

A first estimation of the interaction vertex is obtained by using the clusters on the two layers of SPD. The algorithm matches the clusters on the SPD layers inside a fixed azimuthal window, building a set of segments, called tracklets. Then the space point which minimize the distance from all the tracklets is computed and represents the interaction vertex estimation. At least two tracklets are required for a 3D reconstruction of the primary vertex position. This estimation is very fast, but the most precise determination of the primary vertex position is obtained by using the full reconstructed track information (Figure 2.8b). The full reconstructed tracks, obtained at the end of the tracking procedure, are propagated to the nominal beam line and the tracks too far from it are excluded from the vertex computation.

Secondary vertex reconstruction

Once the tracks and the primary vertex have been reconstructed, the event reconstruction procedure searches for secondary vertices from particle decays. The reconstruction of the secondary vertexes from decays of neutral particles and with a V-shaped track topology of the daughters is performed with the V^0 finder algorithm. The basic principle of the V^0 finder algorithm is the matching of two tracks with opposite sign, which are close in the space and presumably come from the decay of one mother particle. The combined tracks and the resulting mother momentum are requested to pass quality selection criteria before being tagged as V^0 candidate. The V^0 finder algorithm is implemented in the ALICE software and performed with two different procedures, the offline and the on-the-fly.

2.6.3 Particle Identification

One of the main feature of the ALICE experiment is the Particle Identification capability with high resolution. To achieve this performances the information provided by different detectors are combined. For the charged hadron identification the ITS, the TPC, the TOF and the HMPID are used. The ITS and the TPC provide information on the specific energy loss of the tracked charged particles. The TOF detector measures the time of flight and the HMPID, a ring-imaging Cerenkov detector, measuring the Cerenkov angle, gives the $\beta = v/c$ of the particle. Those detectors can be used all together but, most common, the particle identification is performed combining the information provided by just few detector. The choice of which detector to use in a particular analysis is dictated by the subject of the analysis.

TPC particle identification

In the TPC particles are identified by measuring their specific energy loss in the detector gas. Up to 159 padrows measure the charge generated in the gas by the passing particle in the ionization process. This charge is related to the particle energy loss by the value of the detector electric field and by gain factors linked to the detector features. The resulting dE/dx is obtained as the truncated mean of the single padrow measurement.

Particle identification is performed by measuring simultaneously the specific energy loss dE/dx and the momentum of each particle traversing the detector gas. The

energy loss as a function of the momentum in TPC has been parametrized with a function originally proposed by the ALEPH collaboration [29]:

$$f(\beta\gamma) = \frac{P_1}{\beta P_4} \left(P_2 - \beta^{P_4} - \ln \left(P_3 + \frac{1}{(\beta\gamma)^{P_5}} \right) \right), \quad (2.10)$$

where β is the particle velocity, γ is the Lorentz factor and P_{1-5} are the fit parameters, obtained from a fit to the experimental data. Alternatively the response functions have been parametrized using splines as shown in Figure ??a which are provided by the ALICE analysis framework.

Finally, particles are identified following the $n\sigma$ method. This method consists in selecting a fiducial band around the expected energy loss – given by the equation 2.10 or by the splines – for the particle of interest. For each track, the distance from the expected energy loss is computed in terms of number of σ , where σ is the dE/dx resolution obtained with a Gaussian fit to the energy loss distribution at each momentum interval. The dE/dx resolution is about 5.2% in pp collisions and 6% in Pb–Pb collisions. A clear identification of the particle species, with the TPC, is possible up to $p \sim 1\text{GeV}/c$, since at higher momenta the specific energy loss of different particle species are superimposed.

Bibliography

1. Gell-Mann, M. A schematic model of baryons and mesons. *Physics Letters* **8**, 214–215 (1964) (cit. on p. 1).
2. Zweig, G. An SU(3) model for strong interaction symmetry and its breaking. *Developments In The Quark Theory Of Hadrons* **1** (1964) (cit. on p. 1).
3. Zweig, G. An SU(3) model for strong interaction symmetry and its breaking II. *Developments In The Quark Theory Of Hadrons* **1** (1964) (cit. on p. 1).
4. Fritzsch, H. & Gell-Mann, M. Current Algebra: Quarks and What Else? *Proceedings of the XVI International Conference on High Energy Physics* **2**, 135 (1972) (cit. on p. 2).
5. Fritzsch, H. & ans Heinrich Leutwyler, M. G.-M. Advantages of the color octet gluon picture. *Physics Letters B* **47**, 365–368 (1973) (cit. on p. 2).
6. Tanabashi, M., Hagiwara, K., Hikasa, K., et al. Review of Particle Physics. *Physical Review D* **98**, 030001 (3 2018) (cit. on pp. 3, 4).
7. Wilson, K. G. Confinement of quarks. *Physical Review D* **10**, 2445–2459 (8 1974) (cit. on p. 3).
8. Braun-Munzinger, P., Koch, V., Schäfer, T. & Stachel, J. Properties of hot and dense matter from relativistic heavy ion collisions. *Physics Reports* **621**. Memorial Volume in Honor of Gerald E. Brown, 76–126 (2016) (cit. on p. 5).
9. Alford, M. G., Schmitt, A., Rajagopal, K. & Schäfer, T. Color superconductivity in dense quark matter. *Reviews of Modern Physics* **80**, 1455–1515 (4 2008) (cit. on p. 5).
10. Miller, M. L., Reygers, K., Sanders, S. J. & Steinberg, P. Glauber modeling in high energy nuclear collisions. *Ann. Rev. Nucl. Part. Sci.* **57**, 205–243 (2007) (cit. on pp. 6, 7).
11. Gale, C., Jeon, S. & Schenke, B. Hydrodynamic Modelling og Heavy-Hion Collisions. *International Journal of Modern Physics A* **28**, 1340011 (2013) (cit. on p. 9).
12. Kapusta, J. I. Mechanisms for deuteron production in relativistic nuclear collisions. *Physical Review C* **21**, 1301–1310 (4 1980) (cit. on pp. 10, 14).
13. Braun-Munzinger, P., Redlich, K. & Stachel, J. Particle production in heavy ion collisions, 491–599 (2003) (cit. on p. 12).
14. Andronic, A., Braun-Munzinger, P., Stachel, J. & Stocker, H. Production of light nuclei, hypernuclei and their antiparticles in relativistic nuclear collisions. *Physical Letters* **B697**, 203–207 (2011) (cit. on p. 13).

15. ATLAS, Aad, G., et al. Observation of a new particle in the search for the Standard Model Higgs boson with the ATLAS detector at the LHC. *Physics Letters* **B716**, 1–29 (2012) (cit. on p. 15).
16. CMS, Chatrchyan, S., et al. Observation of a new boson at a mass of 125 GeV with the CMS experiment at the LHC. *Physics Letters* **B716**, 30–61 (2012) (cit. on p. 15).
17. LHCb, Aaij, R., et al. Observation of $J/\psi p$ Resonances Consistent with Pentaquark States in $\Lambda_b^0 \rightarrow J/\psi K^- p$ Decays. *Physical Review Letters* **115**, 072001 (7 2015) (cit. on p. 15).
18. Lefèvre, C. *The CERN accelerator complex. Complexe des accélérateurs du CERN* 2008. <<https://cds.cern.ch/record/1260465>> (cit. on p. 16).
19. Evans, L. & Bryant, P. LHC Machine. *JINST* **3**, S08001 (2008) (cit. on p. 17).
20. ALICE, Carminati, F, Foka, P, et al. ALICE: Physics Performance Report, Volume I. *Journal of Physics G: Nuclear and Particle Physics* **30**, 1517 (2004) (cit. on p. 18).
21. ALICE, Fabjan, C. W., et al. ALICE: Physics performance report, volume II. *Journal of Physics G: Nuclear and Particle Physics* **G32** (eds Collaboration, A., Alessandro, B, Antinori, F, et al.) 1295–2040 (2006) (cit. on p. 18).
22. ALICE, Aamodt, K., et al. The ALICE experiment at the CERN LHC. *JINST* **3**, S08002 (2008) (cit. on pp. 18, 21, 22, 24).
23. ALICE, Abelev, B., et al. Performance of the ALICE experiment at the CERN LHC. *International Journal of Modern Physics A* **29**, 1430044 (2014) (cit. on pp. 20, 21, 27).
24. B., A. et al. The construction of the L3 experiment. *Nuclear Instruments and Methods in Physics Research A* **289**, 35–102 (1990) (cit. on p. 19).
25. Fabjan, C. W., Jirdén, L, Lindestruth, V, et al. *ALICE trigger data-acquisition high-level trigger and control system: Technical Design Report* <<https://cds.cern.ch/record/684651>> (CERN, Geneva, 2004) (cit. on p. 24).
26. Frühwirth, R. Application of Kalman filtering to track and vertex fitting. *Nuclear Instruments and Methods in Physics Research A* **262**, 444 –450 (1987) (cit. on pp. 26, 28).
27. *AliEn* <<http://alien.web.cern.ch/>> (cit. on p. 27).
28. *ROOT* <<https://root.cern.ch/>> (cit. on p. 27).
29. Blum, W., Riegler, W. & Rolandi, L. *Particle Detection with Drift Chambers* (Springer-Verlag Berlin Heidelberg, 2008) (cit. on p. 32).